Supporting Information for "Summer-Winter Contrast in the Response of Precipitation Extremes to Climate Change over Northern Hemisphere Land"

Andrew I. L. Williams[1] and Paul A. O'Gorman[2]

[1]Atmospheric, Oceanic and Planetary Physics, Department of Physics, University of Oxford, Oxford, UK

[2]Department of Earth, Atmospheric and Planetary Sciences, Massachusetts Institute of Technology, Cambridge, MA, USA

Contents of this file

Text S1-S3 and Figures S1-S20.

Introduction

This document provides supporting text and figures for the main article.

1. Text S1 describes the CMIP5 models used in this study.

2. Text S2 describes the calculation of the moist stability.

3. Text S3 describes the calculation of CAPE and CIN and their changes.

4. Figures S1-S20 support the findings in the main text.

————

Corresponding author: A. Williams, Department of Atmospheric, Oceanic and Planetary Physics, Department of Physics, University of Oxford, Oxford, UK. (andrew.williams@physics.ox.ac.uk)

Text S1.

We use the following 18 CMIP5 models: ACCESS1-0, ACCESS1-3, BNU-ESM, CMCC-CESM, CMCC-CM, CMCC-CMS, CNRM-CM5, CSIRO-Mk3-6-0, CanESM2, FGOALS-g2, GFDL-ESM2M, IPSL-CM5A-LR, IPSL-CM5A-MR, IPSL-CM5B-LR, MPI-ESM-LR, MPI-ESM-MR, NorESM1-M, bcc-csm1-1-m.

However, Fig. 3 and S9-S15 required RH_{2m} ('hurs') which was only available for the following 12 CMIP5 models: ACCESS1-0, ACCESS1-3, BNU-ESM, CNRM-CM5, CSIRO-Mk3-6-0, CanESM2, GFDL-ESM2M, IPSL-CM5A-LR, IPSL-CM5A-MR, IPSL-CM5B-LR, NorESM1-M, bcc-csm1-1-m.

Text S2.

We examine the fractional changes in 500hPa moist static stability, σ_m, for the same subset of CMIP5 models used in Fig. 3, on the day of the extreme event in JJA. The moist static stability, σ_m, is defined as,

$$\sigma_m = -\frac{RT}{p\theta} \left(\frac{\partial \theta}{\partial p} - \left. \frac{\partial \theta}{\partial p} \right|_{\theta^*} \right),$$

where R is the gas constant for dry air, T is the temperature, θ is the dry potential temperature and $\frac{\partial \theta}{\partial p}|_{\theta^*}$ is the vertical gradient of dry potential temperature for a moist adiabatic lapse rate (assuming constant saturated equivalent potential temperature, θ^*). All quantities are taken on the day of the extreme event in JJA, and the calculation is performed on standard pressure levels. This definition of moist static stability is similar to that used by Tandon et al. (2018) and Li and O'Gorman (2020).

The multi-model mean values of σ_m^e in the control climate (1950-2000) are presented in Fig. S7a and the sensitivities with warming are presented in Fig. S7b. Because the climatological σ_m^e changes sign from negative to positive near our area of interest (the NH midlatitudes), we present absolute rather than percentage trends. Note that in the expression for the change in vertical velocity from the QG-omega equation (Equation 12 from Li and O'Gorman (2020)), the moist static stability appears in the denominator but not on its own, so it is not a problem for it to be zero or weakly negative in the control climatology.

Text S3.

We calculate CIN and CAPE for each of the models included in Fig. 3 using the `xcape` python package (Lepore et al., 2021). CAPE is taken as the vertical integral of the positive buoyancy of a parcel lifted pseudo-adiabatically from the surface, and CIN is defined similarly but for the negative buoyancy. Freezing is treated using a mixed-phase range, with the fraction of ice decreasing linearly from one at -40°C to zero at 0°C. The calculations are performed using daily temperature and specific humidity on pressure levels and at the surface. Daily surface pressure was not available for all of the models and so we used monthly-mean surface pressure. When calculating CIN and CAPE on a given day in JJA, we use monthly surface pressure for the month that contains the day.

Changes in seasonal mean CIN in JJA are shown in Fig. S12 and are correlated with the dynamical contribution both spatially and across models. CIN^e and $CAPE^e$ (which are evaluated on the day of the Rx1day event) and their sensitivities to warming are presented in Fig. S13-S14. CIN^e does increase over NH extratropical land during JJA,
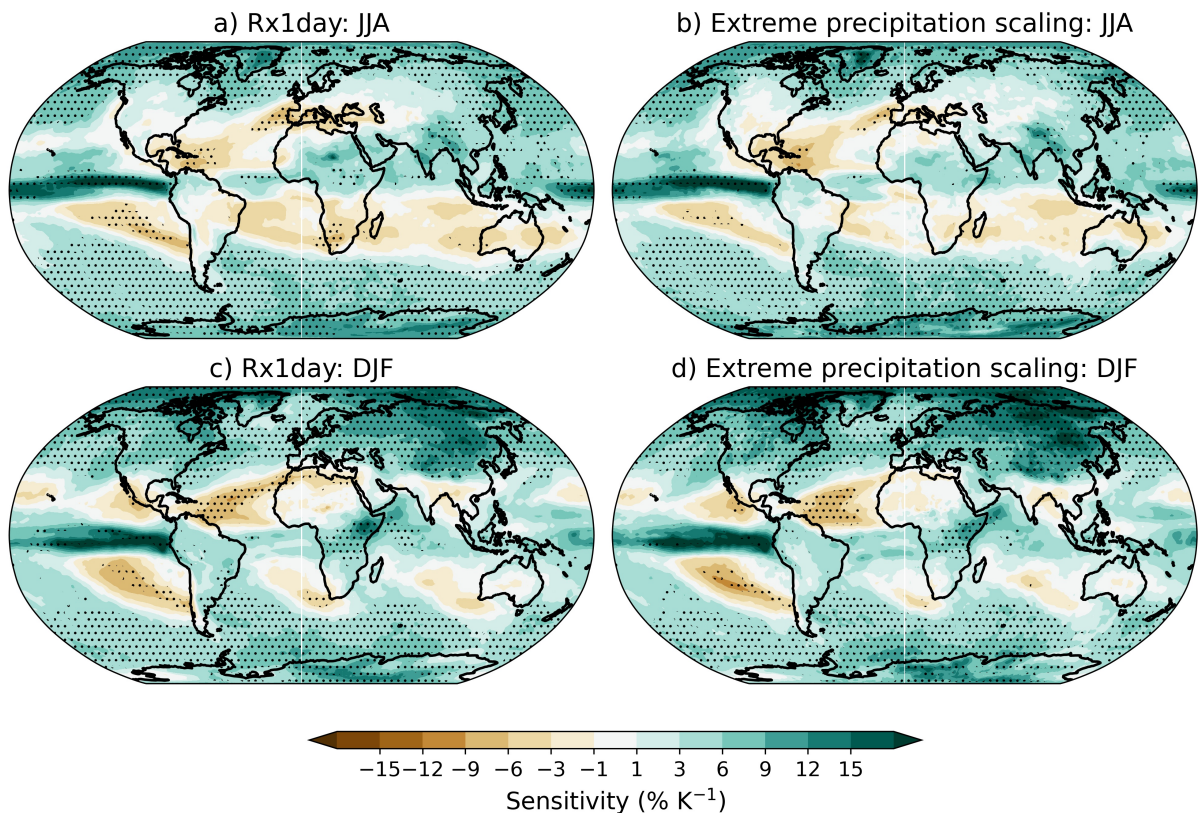
but the increases are weak and not as well correlated with the dynamic contribution (Fig. S14), for reasons that remain unclear.

One alternative mechanism we investigated is that decreases in near-surface relative humidity could inhibit convective heating through entrainment of relatively drier environmental air. The region of decreased RH_{2m}^{e} over NH land extends through the lower troposphere (Fig. S15), but these changes do not correlate very well with inter-model changes in the dynamic contribution (Fig. S16), and it seems likely that a reverse causality is present whereby weaker ascent leads to lower relative humidity in the free troposphere. Overall, these results do not clearly support the convective entrainment mechanism and further study is needed to investigate the influence of CIN and convective entrainment of lower relative-humidity environmental air on the dynamic contribution, ideally using a cloud-resolving model.
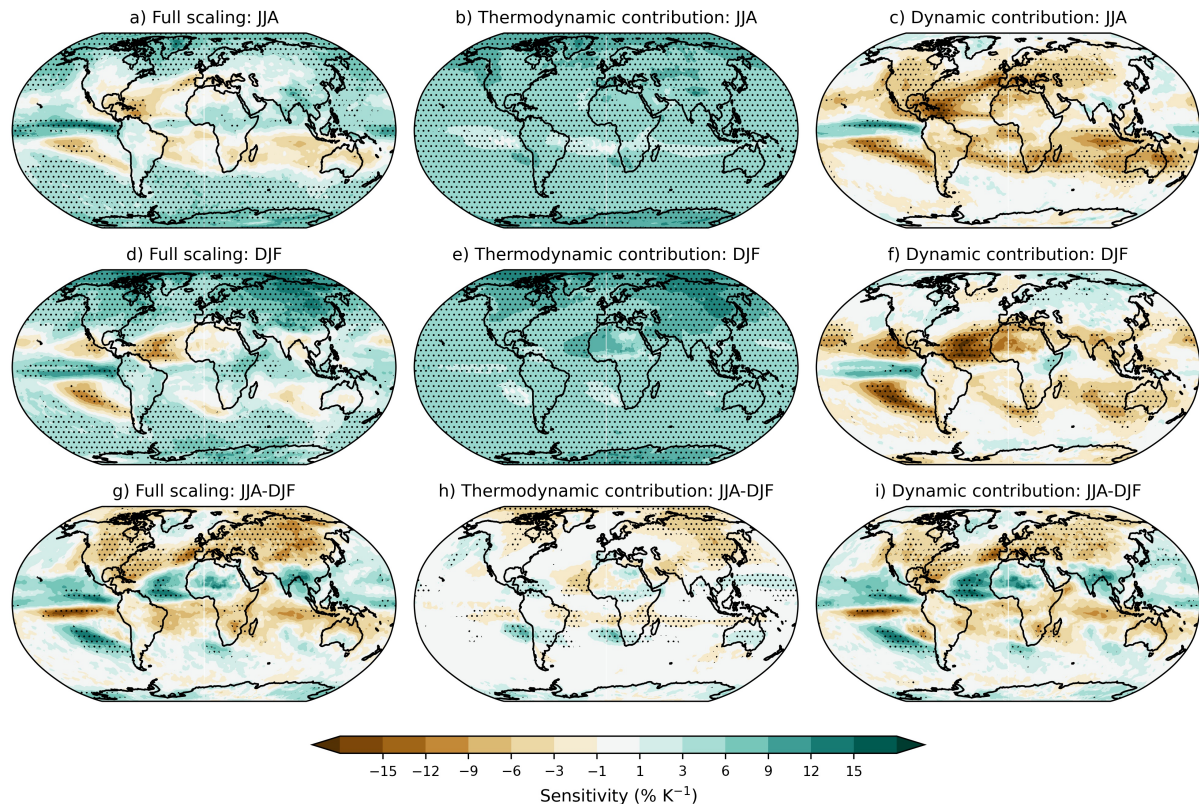
We also find increases in CAPE with warming on the day of the extreme event in JJA (Fig. S13d), which might be thought to imply a positive dynamic contribution. However, previous work has documented a negative dynamic contribution is possible despite CAPE increases (Muller et al., 2011) because CAPE increases with warming mostly reflect increased buoyancy in the upper troposphere (e.g., Singh and O'Gorman (2013)) where specific humidities are small, and thus are not necessarily as important for precipitation extremes.

References
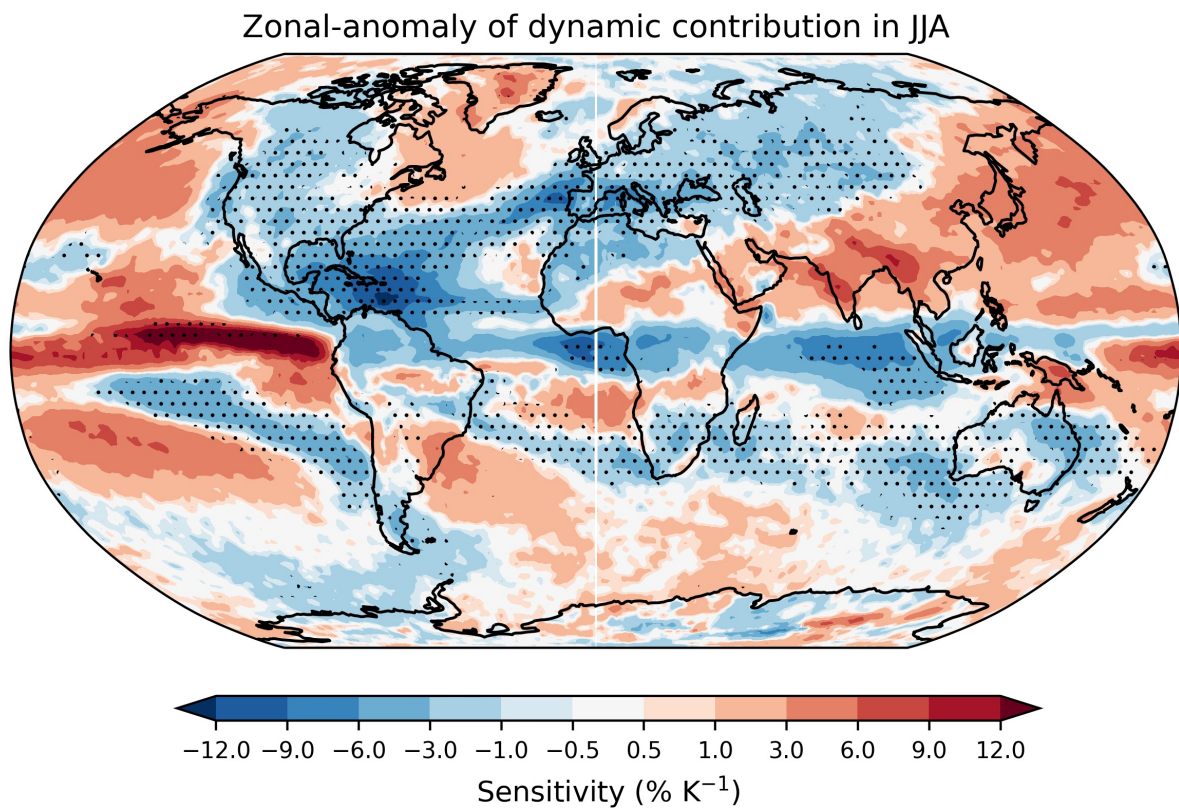
Lepore, C., Allen, J., & Abernathey, R. (2021). *xcape.* Zenodo. doi: 10.5281/zenodo .5270332

Li, Z., & O'Gorman, P. A. (2020). Response of vertical velocities in extratropical precipitation extremes to climate change. *Journal of Climate*, *33*(16), 7125–7139. doi: 10.1175/JCLI-D-19-0766.1

Muller, C. J., O'Gorman, P. A., & Back, L. E. (2011). Intensification of precipitation extremes with warming in a cloud-resolving model. *Journal of Climate*, *24*(11), 2784 - 2800. doi: 10.1175/2011JCLI3876.1

Singh, M. S., & O'Gorman, P. A. (2013). Influence of entrainment on the thermal stratification in simulations of radiative-convective equilibrium. *Geophysical Research Letters*, *40*(16), 4398-4403. doi: https://doi.org/10.1002/grl.50796

Tandon, N. F., Nie, J., & Zhang, X. (2018). Strong influence of eddy length on boreal summertime extreme precipitation projections. *Geophysical Research Letters*, *45*(19), 10,665–10,672. doi: 10.1029/2018GL079327

:
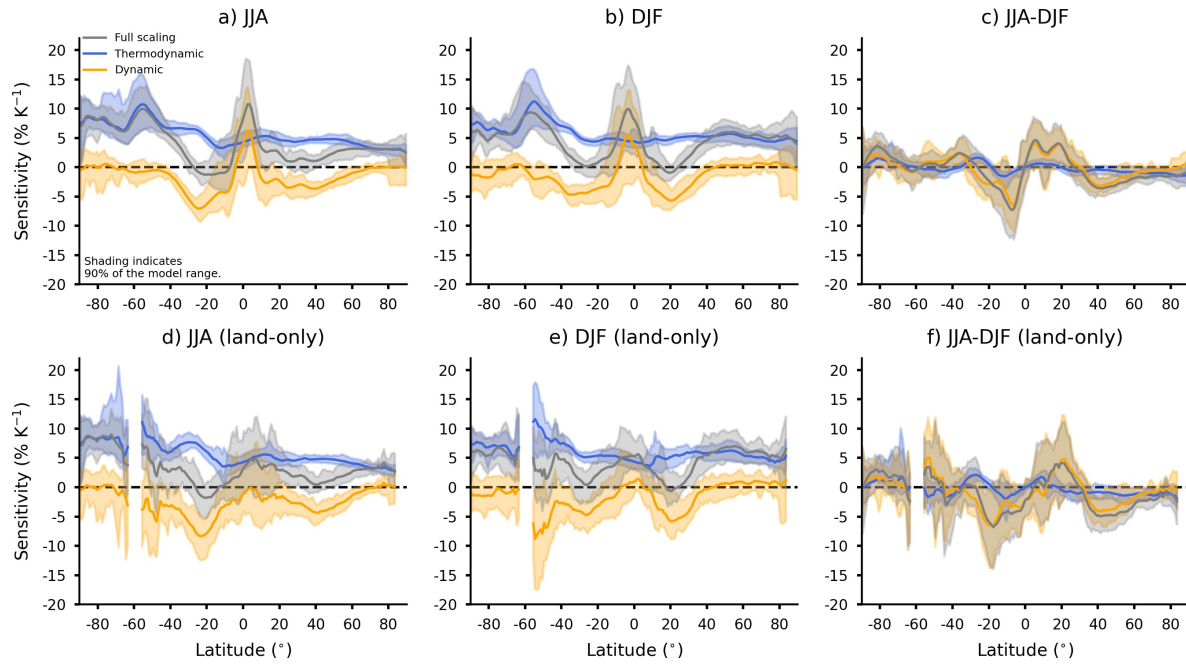
Figure S1. Comparison between CMIP5 multi-model mean changes in seasonal daily maximum precipitation (Rx1day) in JJA (a) and DJF (c) and changes in the corresponding scaling estimate calculated from Eq. 1 in the main text (b, d). Stippling indicates where at least 90% models agree on the sign of the change.
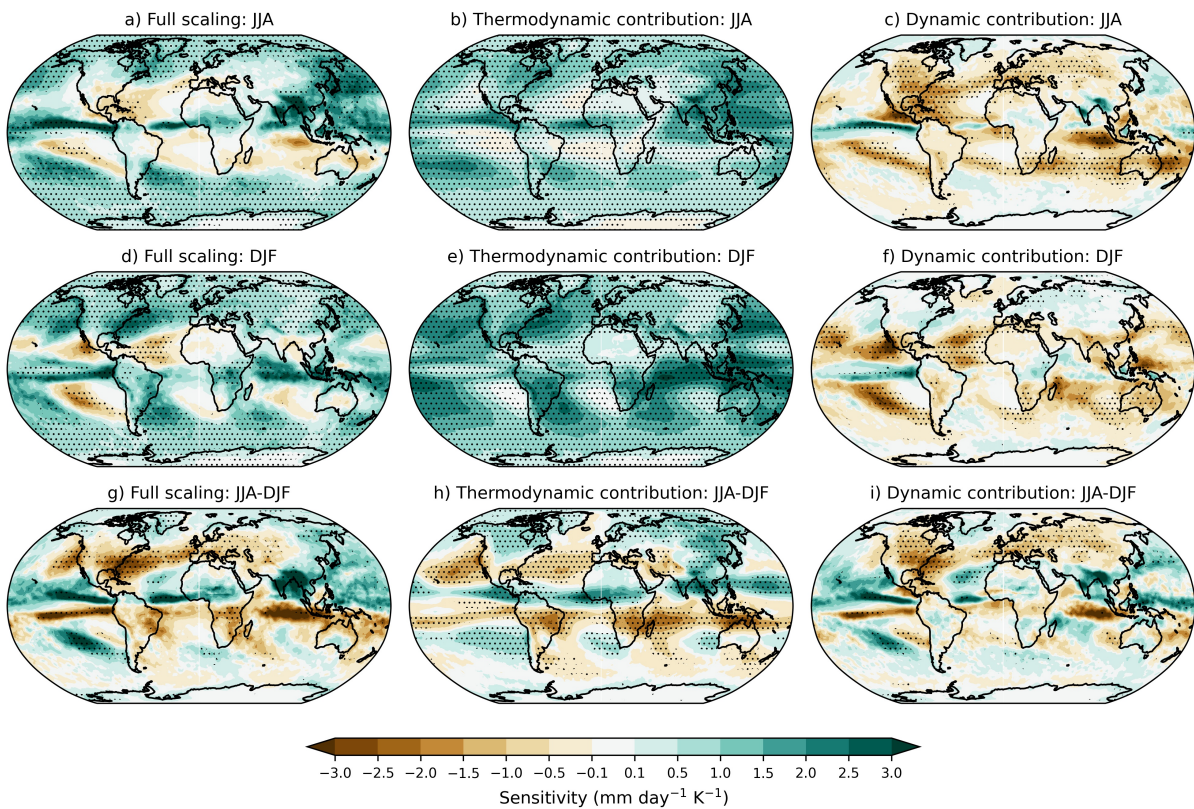
Figure S2. As in Fig. 1 except that the normalization is over the period 1950-2100 instead of 1950-2000. The results are generally similar to the results in Fig. 1.

:

Zonal-anomaly of dynamic contribution in JJA
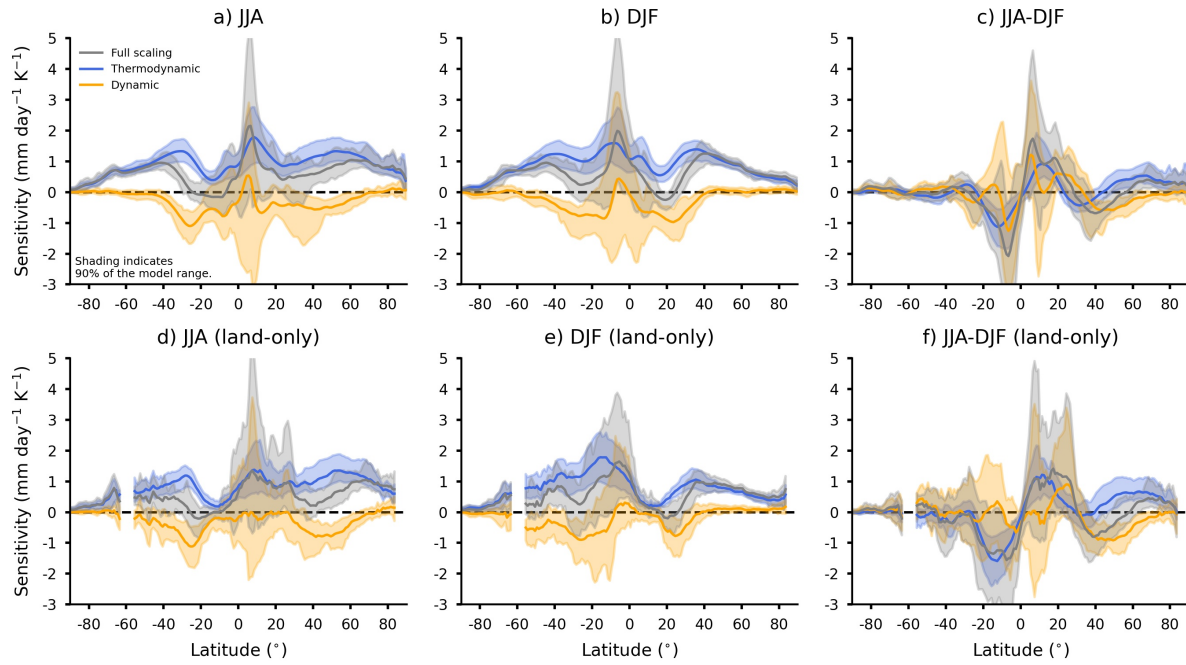
Figure S3. As in Fig. 1c except we plot the anomaly from the zonal mean.
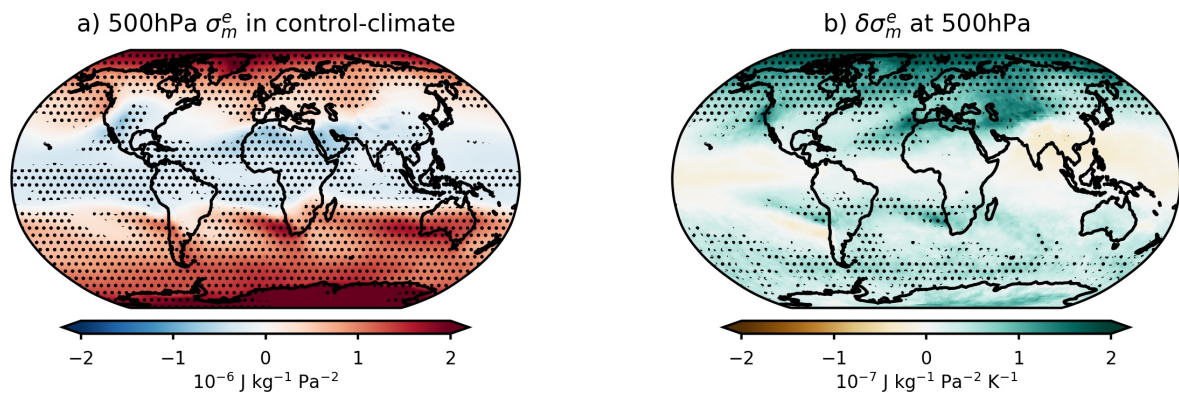
Figure S4. As in Fig. 2 except that here we show the sensitivity with respect to changes in zonal-mean temperature change rather than global-mean temperature change. There is a JJA-DJF contrast over NH extratropical land, driven by the dynamic contribution, which is robust across the CMIP5 models considered. The main difference from Fig. 2 is that the JJA-DJF contrast in the thermodynamic contribution is substantially weaker when regressing against zonal-mean temperature.
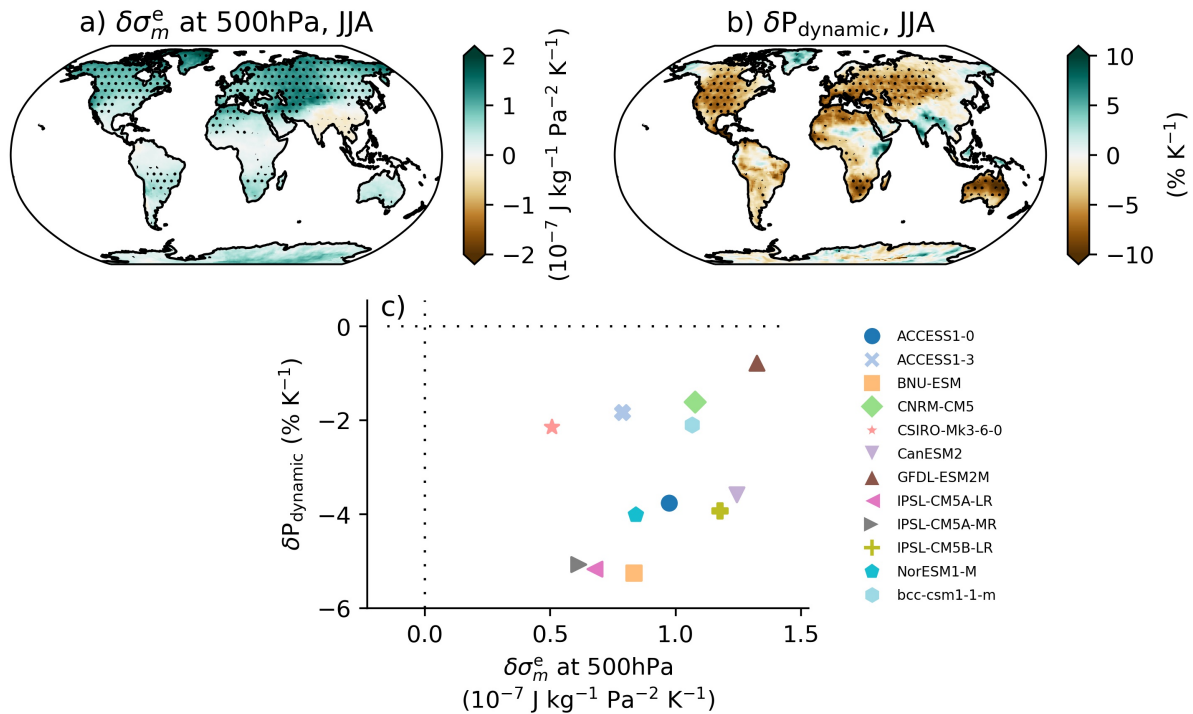
Figure S5.   As in Fig. 1 except that here we do not normalize the daily maximum time-series by their average over the 1950-2000 period, and thus the trends are in mm day^{-1} K^{-1} as opposed to % K^{-1}. There is still a JJA-DJF contrast in changes in precipitation extremes over much of NH midlatitude land but not to the same extent as when percentage changes are considered.
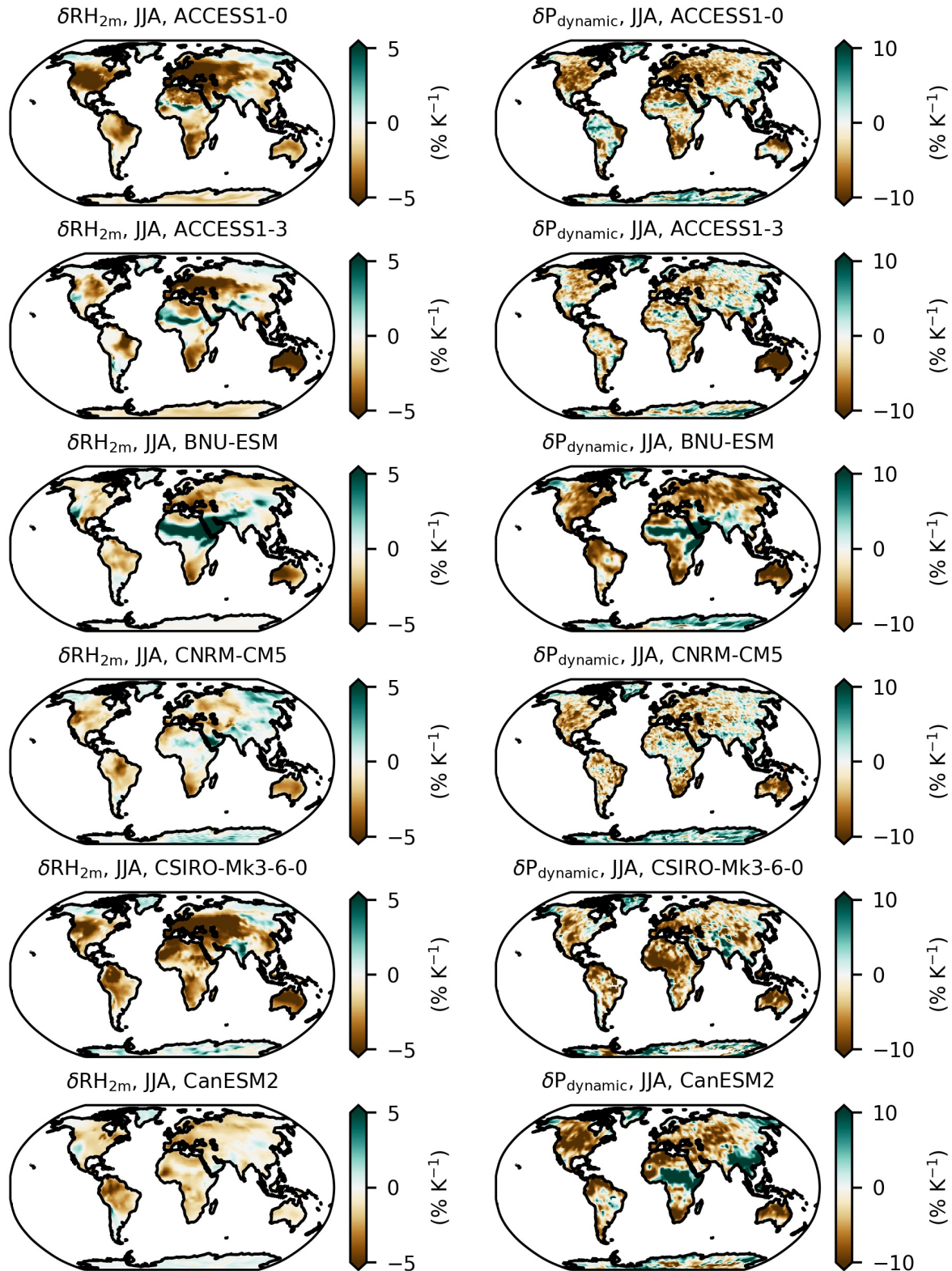
Figure S6. As in Fig. 2 except that here we do not normalize the daily maximum time-series by their average over the 1950-2000 period, and thus the trends are in mm day^{-1} K^{-1} as opposed to % K^{-1}. This figure demonstrates that while the dynamic contribution still contributes to a JJA-DJF contrast over the NH in absolute terms, it is largely cancelled out in the zonal mean at higher latitudes by weaker thermodynamic trends in DJF than in JJA.

:

a) 500hPa σ_m^e in control-climate

b) $\delta\sigma_m^e$ at 500hPa

10^{-6} J kg^{-1} Pa^{-2}

10^{-7} J kg^{-1} Pa^{-2} K^{-1}
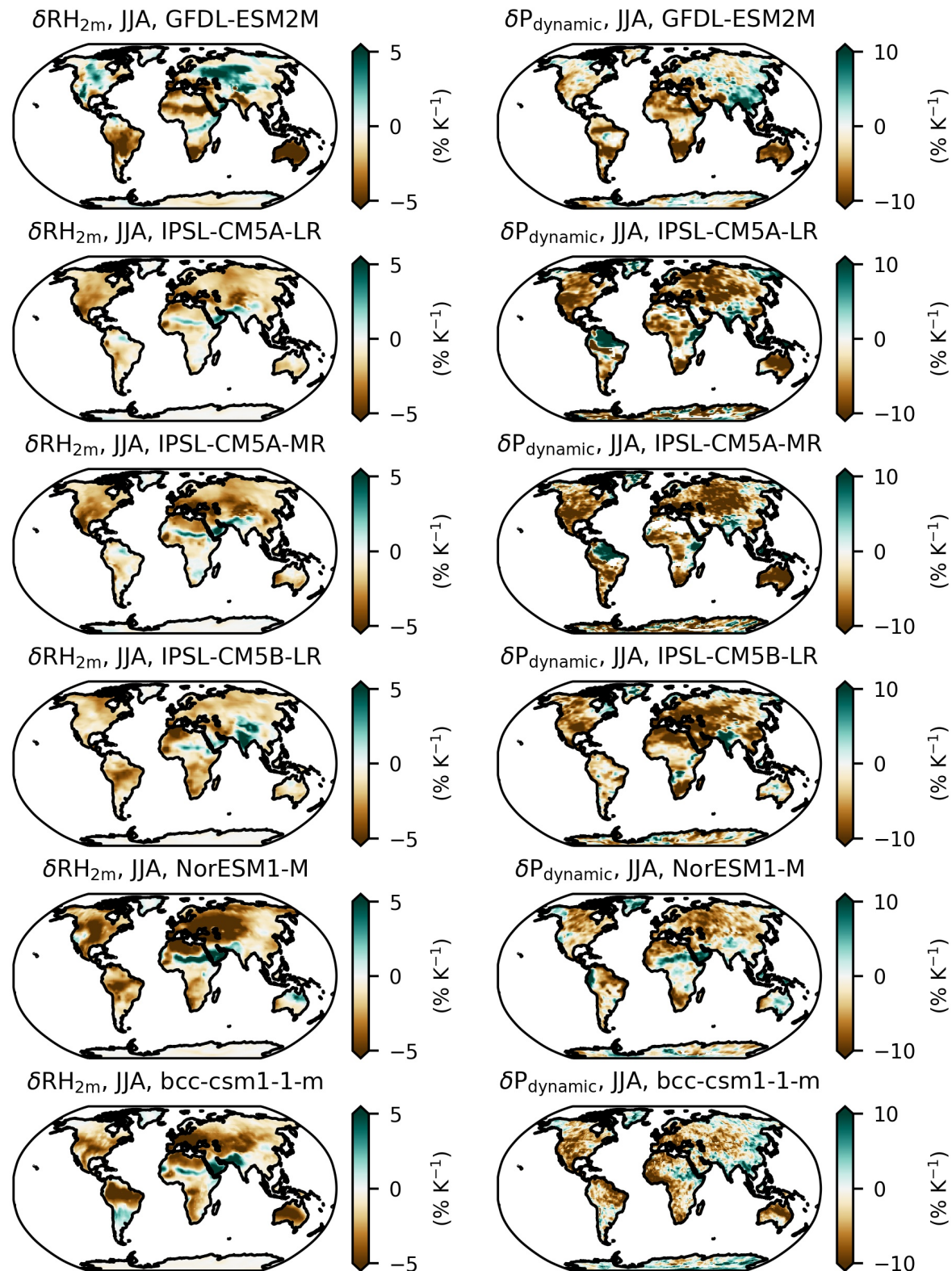
Figure S7. (a) Multi-model mean moist static stability, σ_m^e, at 500hPa calculated on the day of the extreme event in JJA and then averaged from 1950-2000. (b) Sensitivity of σ_m^e at 500hPa to global-mean warming, where absolute rather than fractional changes are used here because σ_m^e changes sign in the NH midlatitudes in the control-climate. Stippling indicates 90% model agreement.
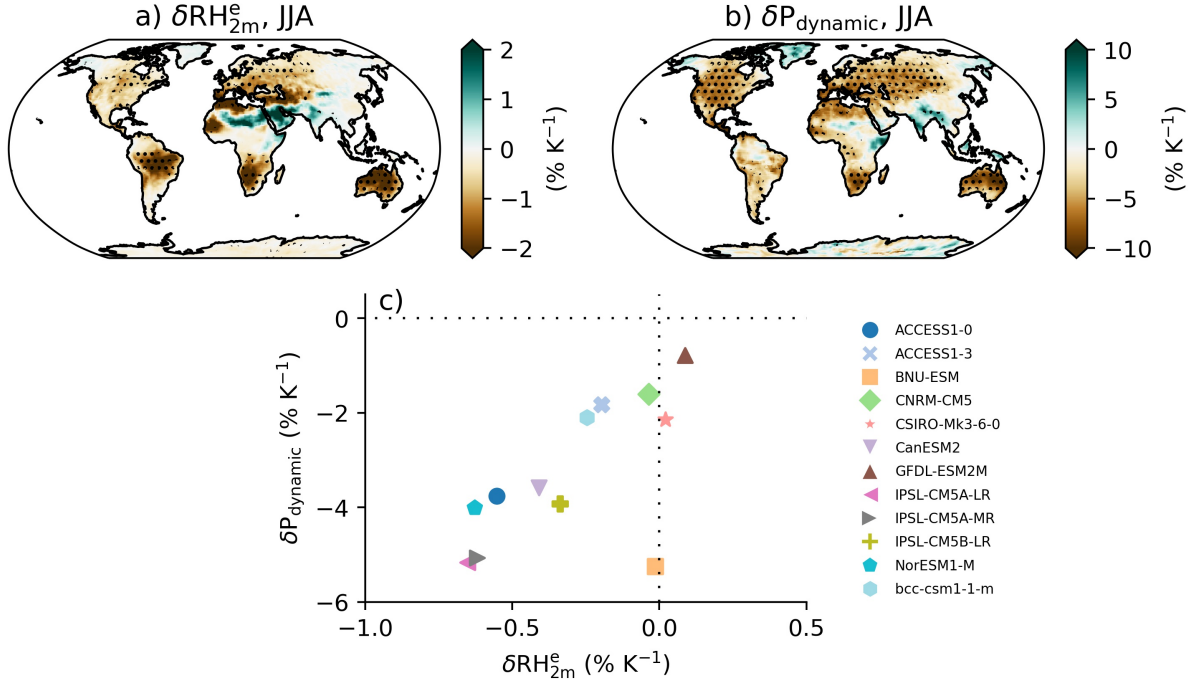
Figure S8.   As in Fig. 3 except we have replaced seasonal-mean surface relative humidity with moist static stability at 500hPa on the day of the extreme event, σ_m^e. Note that absolute rather than fractional changes in σ_m^e are used to define its sensitivity to warming. The results show that σ_m^e changes correlate with the dynamic contribution in terms of spatial pattern but not inter-model scatter. (Note that in panel c there is a hint that a more negative dynamic contribution is associated with a smaller increase in moist static stability, but this is the opposite of what would be expected from a physical point of view.)

:
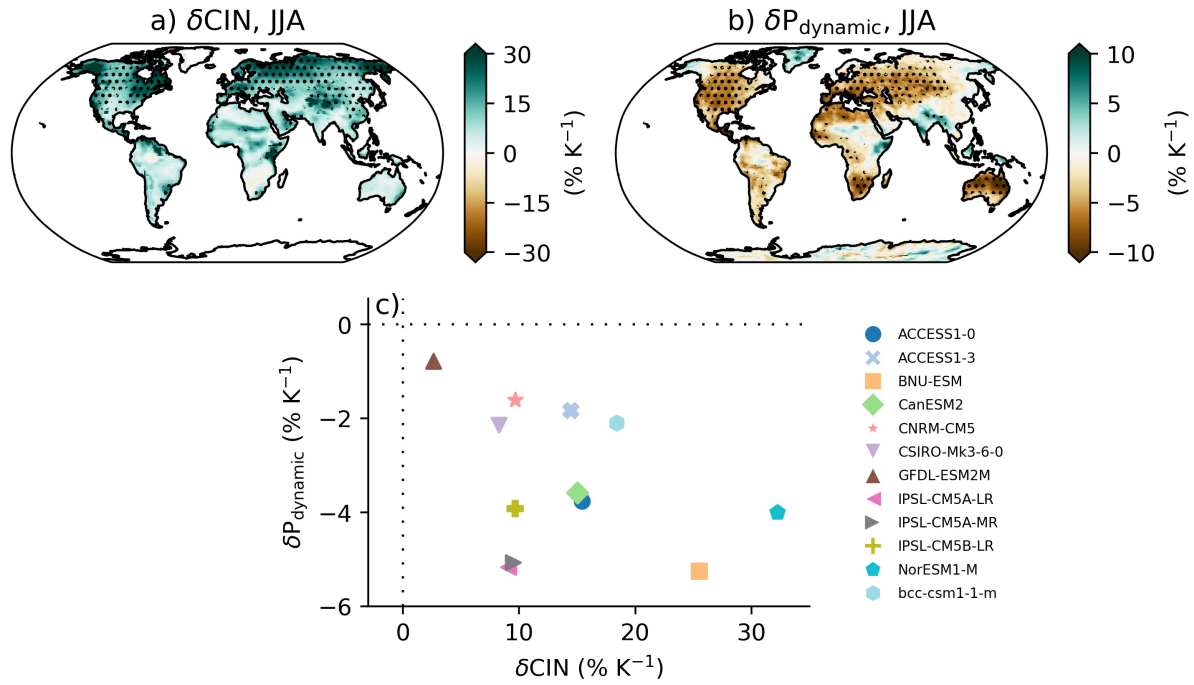
Figure S9. As in Fig.3a,b except showing the first six CMIP5 models individually.

δRH$_{2m}$, JJA, GFDL-ESM2M

δP$_{dynamic}$, JJA, GFDL-ESM2M

δRH$_{2m}$, JJA, IPSL-CM5A-LR

δP$_{dynamic}$, JJA, IPSL-CM5A-LR

δRH$_{2m}$, JJA, IPSL-CM5A-MR

δP$_{dynamic}$, JJA, IPSL-CM5A-MR

δRH$_{2m}$, JJA, IPSL-CM5B-LR

δP$_{dynamic}$, JJA, IPSL-CM5B-LR

δRH$_{2m}$, JJA, NorESM1-M

δP$_{dynamic}$, JJA, NorESM1-M

δRH$_{2m}$, JJA, bcc-csm1-1-m

δP$_{dynamic}$, JJA, bcc-csm1-1-m
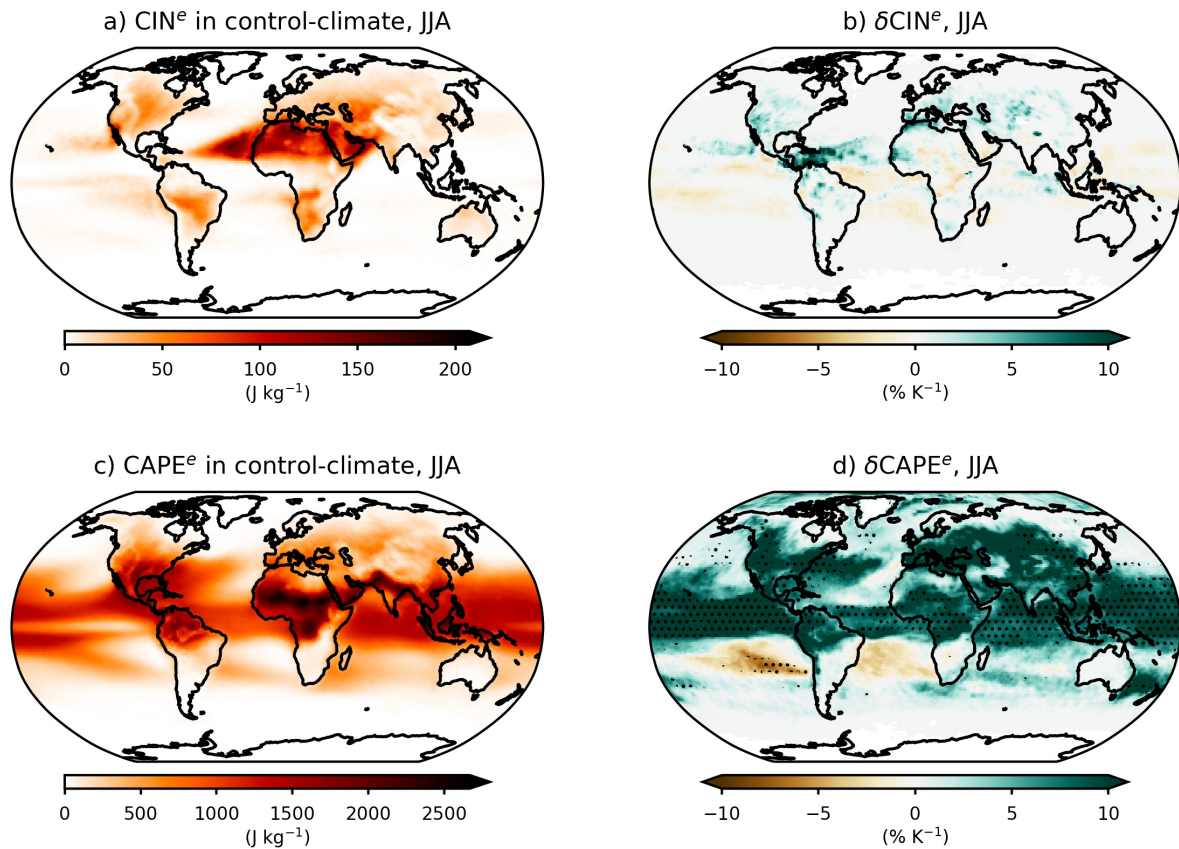
Figure S10.   As in Fig.3a,b except showing the last six CMIP5 models individually.

a) δRH_{2m}^e, JJA

b) $\delta P_{dynamic}$, JJA

c)
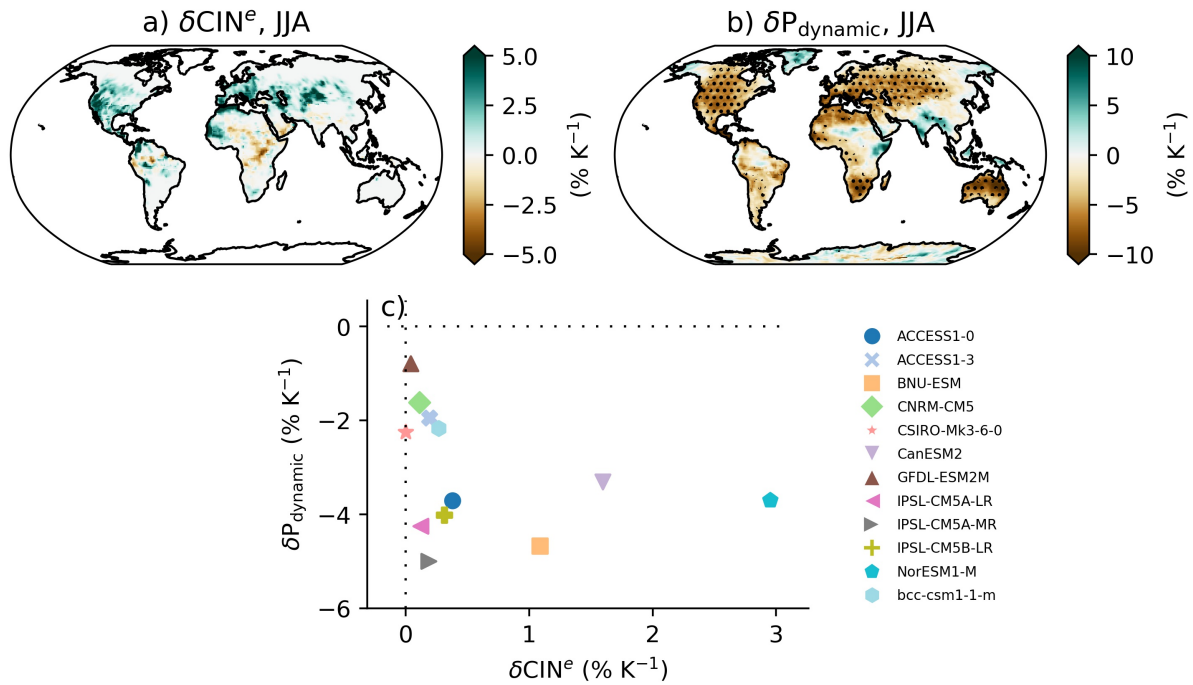
Figure S11. As in Fig. 3 of the main text, except we use RH_{2m} on the day of the extreme event in JJA (denoted using a superscript ^{e}), as opposed to the seasonal-mean RH_{2m}. The correlation in panel c is improved when we make this change, except for one outlier. However, RH_{2m}^e captures less of the spatial pattern and pattern of model agreement than seasonal-mean RH_{2m} over NH land.
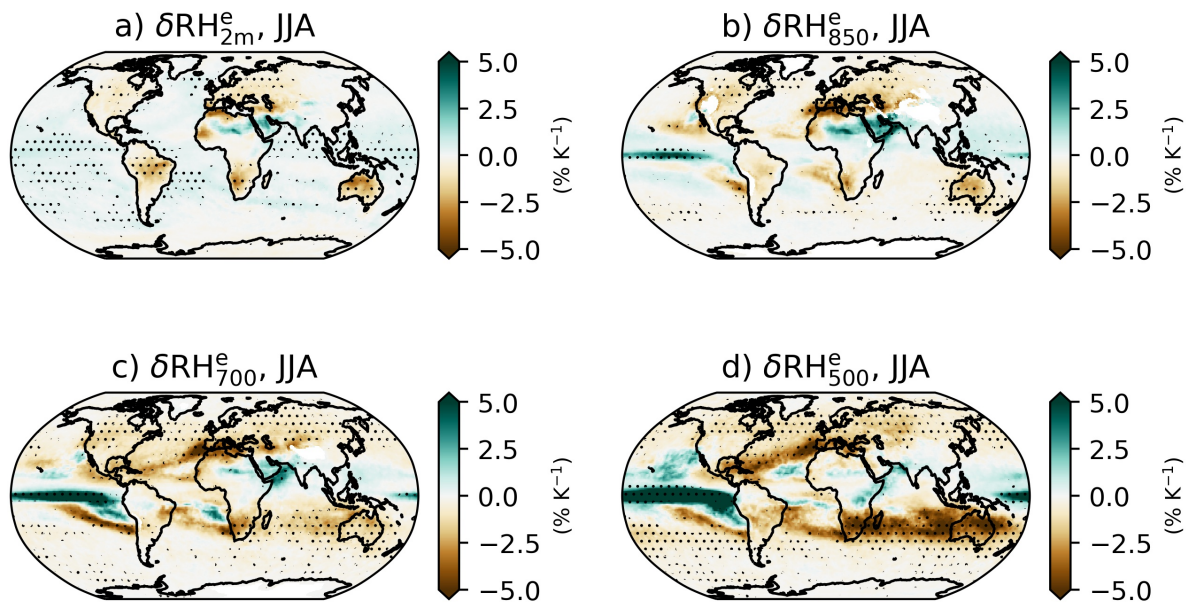
Figure S12. As in Fig. 3 of the main text, except we have replaced seasonal-mean RH$_{2m}$ with seasonal-mean CIN. Seasonal-mean changes in CIN during JJA capture much of the spatial pattern of the dynamic contribution over NH land, and they also capture much of the inter-model spread in the dynamic contribution.
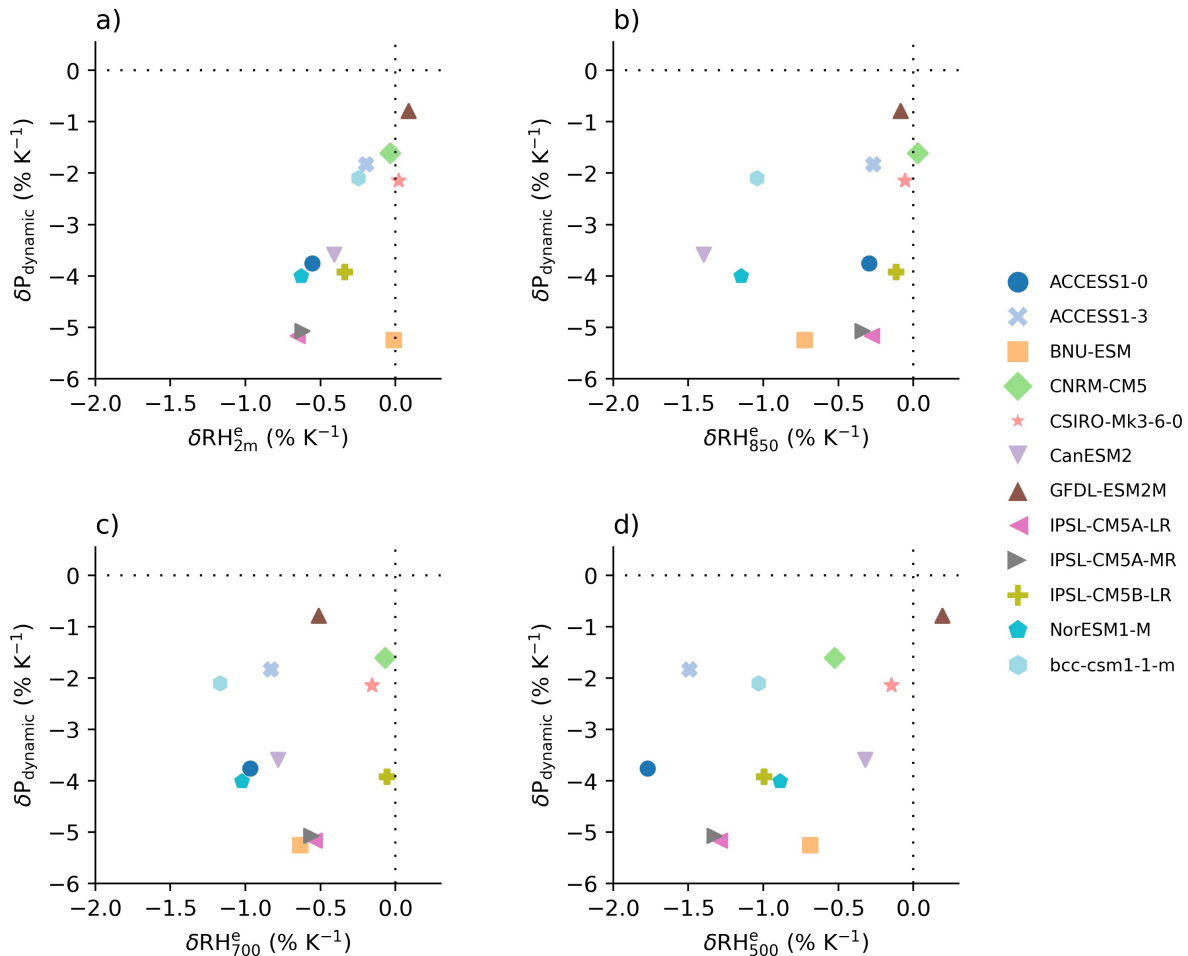
Figure S13. (a,c) Multi-model mean CAPE and CIN calculated on the day of the extreme event in JJA (denoted using a superscript ^{e}) and then averaged from 1950-2100. (b,d) Sensitivities of CIN^e and $CAPE^e$ to warming, where stippling indicates 90% of models agree on the sign of the change.
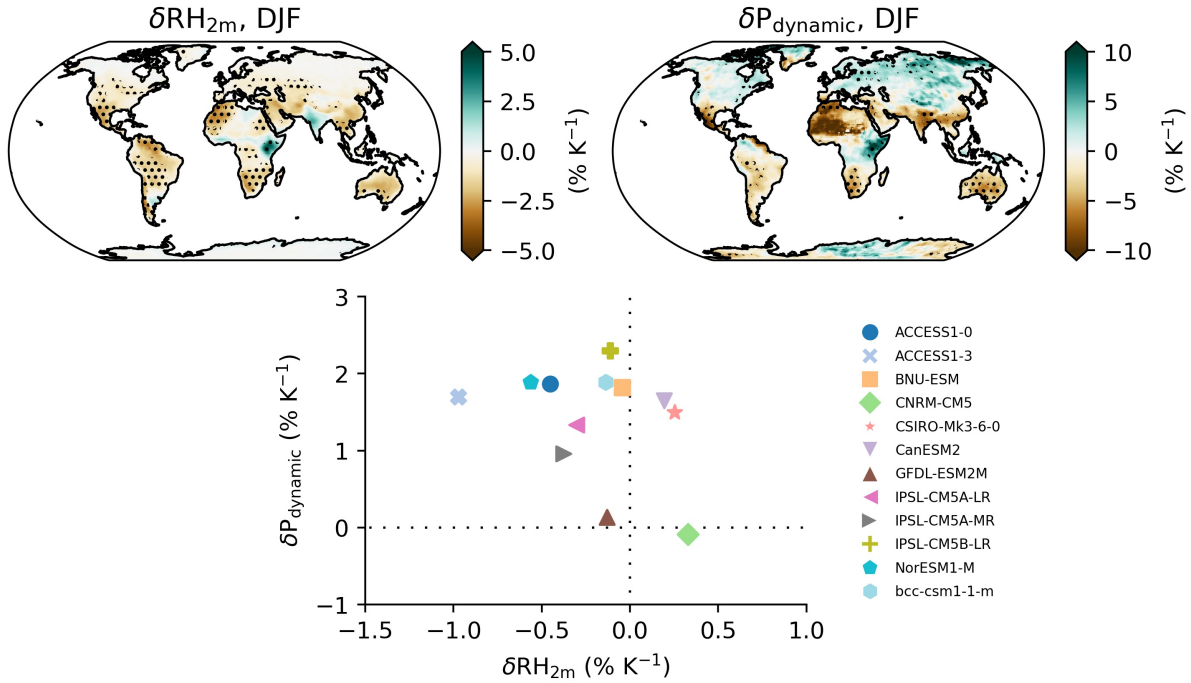
Figure S14. As in Fig. 3 of the main text, except we we have replaced seasonal-mean RH$_{2m}$ with CIN calculated on the day of the extreme event in JJA (denoted using a superscript ^{e}). In panel (c) we calculate the scatter plot using the mean trends across 40-70°N land as opposed to using the median (as in previous figures). This is because most models exhibit negligible δCIN^e trends during JJA for greater than half of the grid-points over NH extratropical land, and so the median does not represent the inter-model scatter as faithfully as the mean.

:
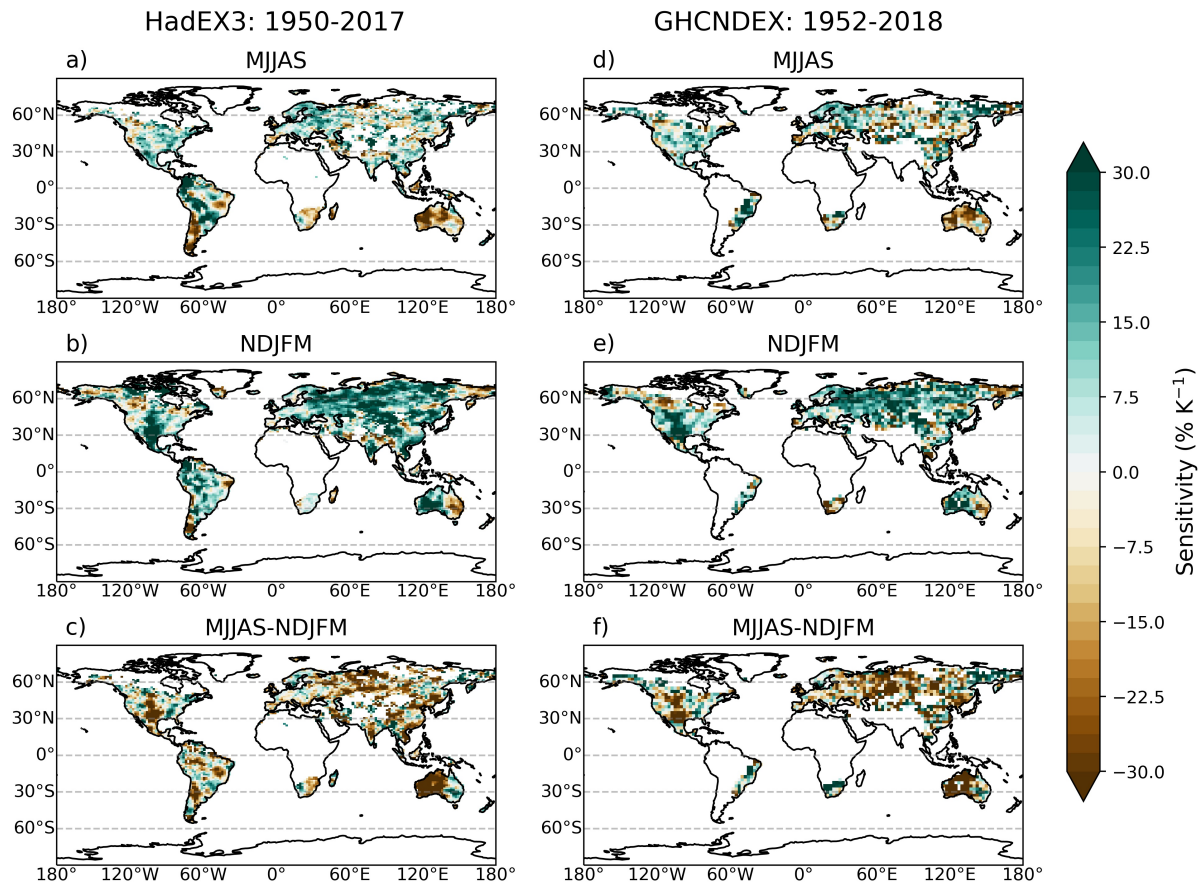
Figure S15. The spatial pattern of fractional changes in relative humidity on the day of the extreme event in JJA for changes at (a) the surface, (b) at 850hPa, (c) at 700hPa and (d) at 500hPa. Stippling indicates 90% of models agree on the sign of the change.
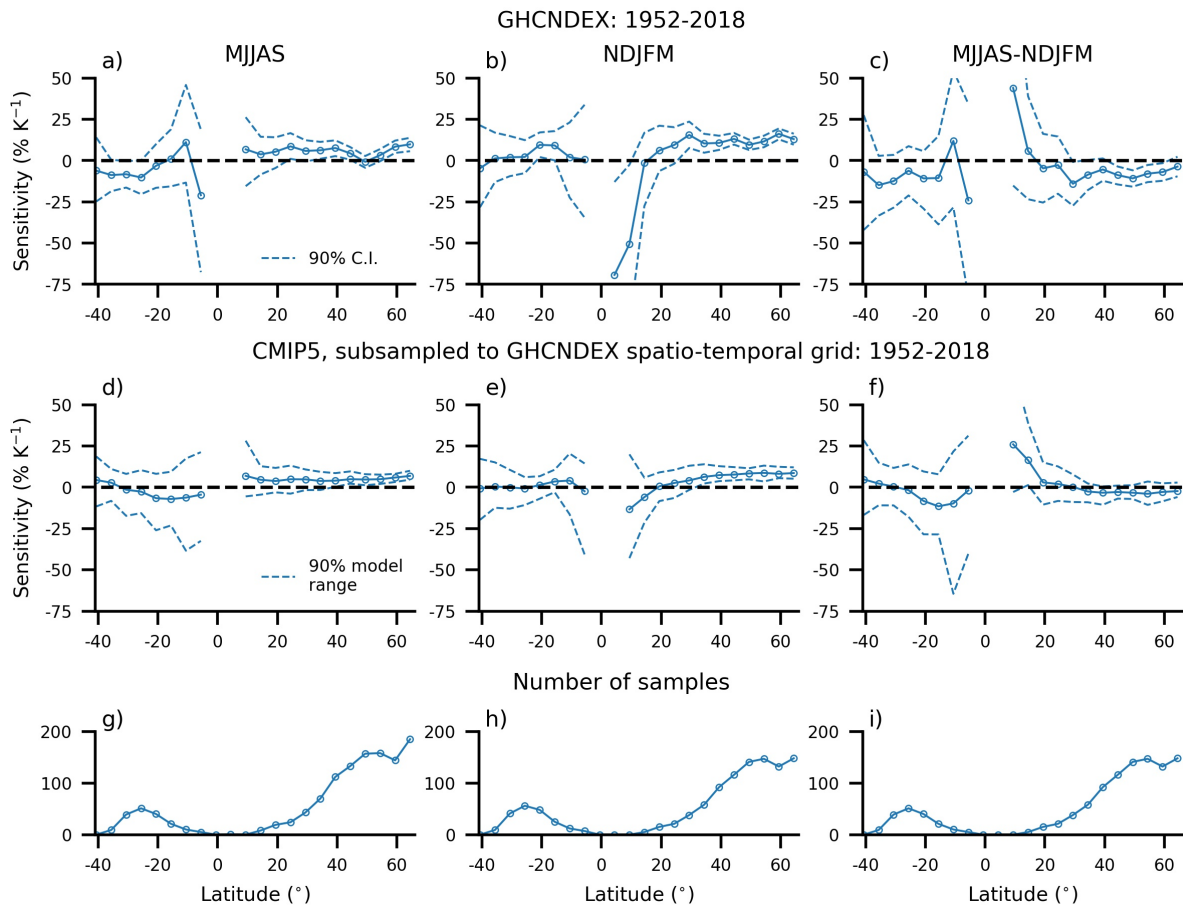
Figure S16.   As in Fig. 3c but for fractional changes in the dynamic contribution versus fractional changes in relative humidity at (a) the surface, (b) at 850hPa, (c) at 700hPa and (d) at 500hPa. We calculate the scatter plot by taking the median sensitivities for both quantities across 40-70°N land for JJA.
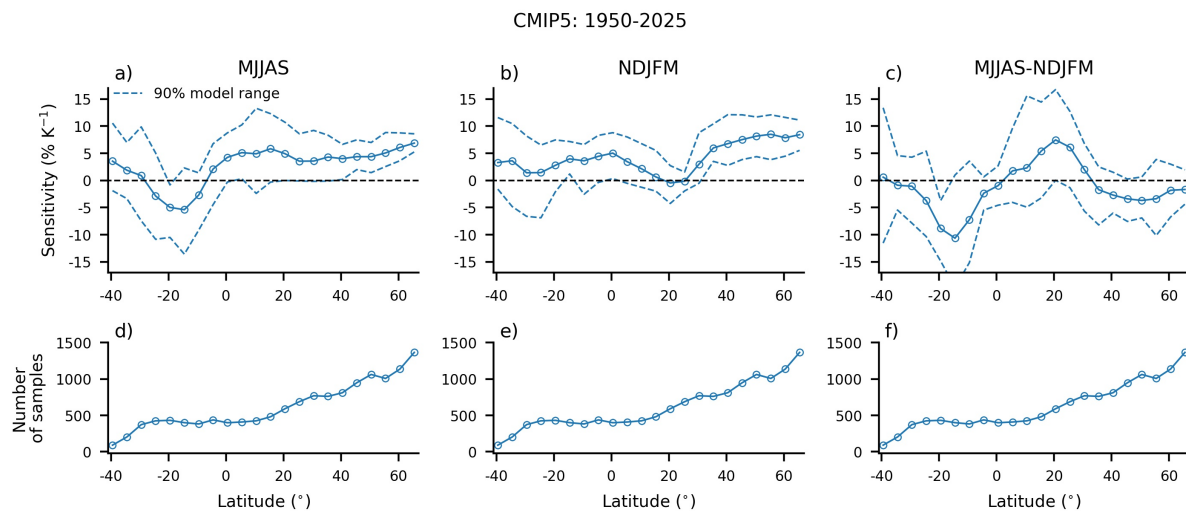
Figure S17. As in Fig. 3, but for DJF. Most models predict a weak decrease in near-surface relative humidity with warming over Northern Hemisphere land in DJF, but the dynamic contribution over Northern Hemisphere land is positive in this season. The lack of a correlation with near-surface relative humidity over the Northern Hemisphere during DJF is likely because precipitation extremes during DJF are associated with weather systems that are less strongly influenced by convection than during JJA.

Figure S18. Regional sensitivities of Rx1day to global temperature changes over the period 1950-2017 for HadEX3 (a,b,c) and 1952-2018 for GHCNDEX (d,e,f). Sensitivities are plotted for (a,d) MJJAS and (b,e) NDJFM for grid boxes with at least 45 years of data, and (c,f) for the seasonal contrast, MJJAS-NDJFM, for grid boxes with at least 45 years with data for both MJJAS and NDJFM (see Section 2 of main text for details). The HadEX3 and GHCNDEX datasets have spatial resolutions of 1.25°x1.875° and 2.5°x2.5°, respectively. The figure shows that HadEX3 has substantially more grid boxes with data in the tropics. Visually it is also apparent that the extreme precipitation sensitivity is lower during MJJAS (a, d) than in NDJFM (b, d) in both datasets over the extratropical Northern Hemisphere, corresponding to a summer-winter contrast over this region (c, f).

Figure S19. As in Fig. 4, except for the GHCNDEX observational dataset rather than HadEX3. CMIP5 simulations are subsampled to GHCNDEX in making this figure.

Figure S20. Sensitivity of seasonal Rx1day over land to warming in CMIP5 over the period 1950-2025 for (a) MJJAS, (b) NDJFM and (c) MJJAS-NDJFM. The sensitivities are calculated the same way as in Fig. 4 and Fig. S17 except for here we do not subsample the CMIP5 models to the spatio-temporal grid of the observations. The results show that the summer-winter contrast is also present in CMIP5 models when there is no missing data. The number of included gridboxes (d,e,f) is the same in each season, but there are latitudinal variations which reflect the fact there is less land in some 5° latitude bands than in others.